J. Fluid Mech. (2005), *vol.* 539, *pp.* 199–227. © 2005 Cambridge University Press
doi:10.1017/S0022112005005641 Printed in the United Kingdom

Experimental study on mean velocity and turbulence characteristics of plane Couette flow: low-Reynolds-number effects and large longitudinal vortical structure

By OSAMI KITOH[1], KOICHI NAKABYASHI[2] AND FUTOSHI NISHIMURA[3]

[1]Department of Engineering Physics, Electronics and Mechanics, Nagoya Institute of Technology,
Gokisocho, Showaku, Nagoya, 466-8555, Japan

[2]Department of Mechanical System Engineering, Aichi University of Technology, 50-2 Manori,
Nishihazama-cho, Gamagori City, Aichi, 443-0047, Japan

[3]Research Institute of Industrial Products, Gifu Prefectual Government, 47 Kitaoyobi,
Kasamatsu Town, Hashima-gun, Gifu, 501-6064, Japan

(Received 18 February 2004 and in revised form 8 April 2005)

Experimental work to investigate plane Couette flow has been performed in the Reynolds number range of $750 \leqslant Re\,(=hU_b/(2\nu)) \leqslant 5000$ or $50 \leqslant Re_*\,(=hu_*/\nu) \leqslant 253$, where U_b, u_* and h are moving wall speed, friction velocity and channel half-height, respectively. The low-Reynolds-number effect on the wall friction coefficient C_f, mean velocity profile and statistical turbulence quantities is discussed in relation to the turbulent Poiseuille flow properties. Since the shear stress is constant in Couette flow, the flow is free from the effect of shear stress gradient and the Reynolds number effect therefore can be seen explicitly, uncontaminated by this effect. A flow region diagram is given to show how the low-Reynolds-number effect penetrates into the wall region. The area of the buffer region is contracted by the low-Reynolds-number effect when $Re_* \leqslant 150$, so that the additive constant B of the log law decrease as Re_* decreases. Also, C_f has a larger value than in Poiseuille flow in the low Re_* range. The log-law area in Couette flow is 2–3 times as wide as that in Poiseuille flow. The defect law is Re_*-dependent and the non-dimensional velocity gradient at the core, $Rs = (\mathrm{d}U_1/\mathrm{d}x_2)(h/u_*)$, increases from 3 to 4.2 as Re_* increases from 50 to 253. The peak value of streamwise turbulence intensity u_{1p}^+ has a constant value of 2.88 but decreases sharply as Re_* reduces below 150.

The large longitudinal vortices extending the entire height of the channel are shown to be sustained in Couette flow that is oscillating around their average position. This causes a slow fluctuation with large amplitude in the streamwise velocity component. These vortices make the Couette flow three-dimensional and the skin friction coefficient varies 20 % sinuously in the spanwise direction, for example. Also, the zero-crossing time separation of streamwise velocity auto-correlation $R_{11}(\tau)$ becomes longer as $\tau = 40h/U_b$, which is 3 times as long as that in Poiseuille flow.

1. Introduction

Couette flow (C-flow) has many special characteristics due to its simple flow geometry and simple dynamical structure and can be considered as the canonical wall turbulent flow together with plane Poiseuille flow (P-flow) as well as turbulent boundary layer flow over a flat plate. From these flows we can extract much basic and important information concerning the characteristics and structure of turbulence, which can contribute greatly to our understanding of wall turbulence and to developing turbulence modelling. Among these flows, extensive research efforts have been aimed toward P-flow and turbulent boundary layer flows. Only a limited number of works, however, in particular experimental, have been reported so far on C-flow.

Excellent reviews of the development of C-flow research are given in Komminaho, Lundbladh & Johansson (1996) and Bech *et al.* (1995) and will not be repeated here. Recent DNS by Bech *et al.* (1995) Komminaho *et al.* (1996) and Andersson, Bech & Kristoffersen (1992) have revealed some important characteristics of C-flow, about which physical experiments could not contribute much. For example, the detailed turbulent kinetic energy budget, the instantaneous streamwise vortical structure in the central region and the role of coherent structures in the near-wall region were discussed. From these works many questions arise that should be more thoroughly studied. Andersson *et al.* pointed out that the standard gradient-type turbulent diffusion model needs modification to realize the diffusion process in the core region where the turbulence intensity is almost constant, i.e. zero gradient but still with non-negligible diffusion. Lee & Kim (1991) reported that quasi-steady large-scale streamwise vortical structures exist in the central part of the channel, but Komminaho *et al.* (1996) pointed out that Lee & Kim's computational domain was too small to cover the long-existing large correlation along the streamwise direction in C-flow. They performed DNS with a sufficiently long (28π times half-channel height in the streamwise direction) computational domain and obtained similar vortical structures that were neither stationary nor fixed in position. Combined with this vortex motion, they also showed large elongated streaky structures of streamwise velocity aligned in the main flow direction. The mechanism of generating and sustaining these vortical structures, however, has not yet been clarified. These types of longitudinal vortex and streaky structures can be seen in various turbulent shear flows. Lee, Kim & Moin (1990) reported longitudinal streaky structures in homogeneous turbulent shear flow, while Carruthers *et al.* (1991) conjectured the existence of coherent structures there. Also, the quasi-streamwise vortex and coherent structures are the basic mechanisms for sustaining wall turbulent flow. Each has its own particular vortex pattern, zig-zag or long and straight in the streamwise direction, due to the different boundary conditions attached to each flow. Hamilton, Kim & Waleffe (1995) performed DNS of a minimal Couette channel to study the regeneration mechanism of the streak and streamwise vortex in the central area of the channel, which is considered to be the same as the mechanism that sustains wall turbulence.

The Reynolds number is the only parameter for C-flow, compared with two parameters for Couette–Poiseuille flow (CP-flow) and P-flow, in which the shear stress gradient parameter μ (to be introduced in §2) plays an important role in addition to the Reynolds number. Figure 1 shows the parameter plane (μ, Re_*) for CP-flow where $Re_* = hu_*/\nu$, h being the half-height of the channel, u_* the friction velocity and ν kinematic viscosity. CP-flow can be classified into P-type flow and C-type flow, Nakabayashi, Kitoh & Katoh (2004). C-flow, a special case of CP-flow, has an infinite value for $|\mu|$ and is free from the μ-effect. P-flow can be realized on a line of $Re_* = -\mu$. The difference of these parameter dependences between C-flow and CP-flow or P-flow makes the Reynolds number effect appear somewhat different. For instance, Komminaho *et al.* (1996) pointed out that for the turbulence characteristics

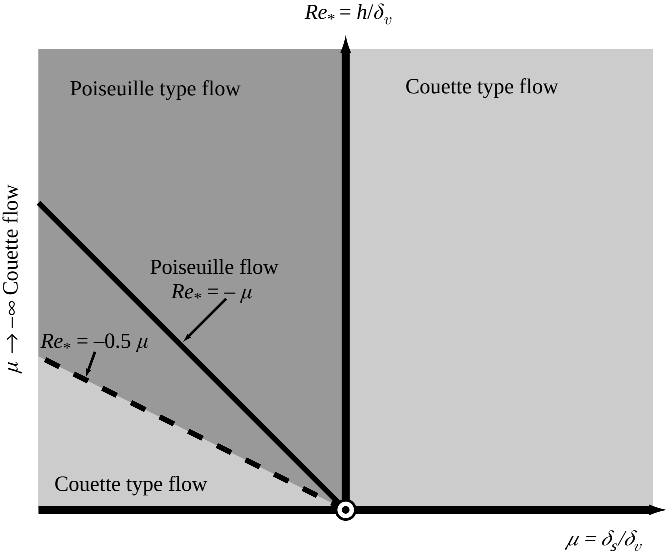

FIGURE 1. Parameter plane for Couette–Poiseuille flow.

near the wall, C-flow is similar to high-Reynolds-number P-flow even though the Reynolds number itself is low. Since the Reynolds numbers of DNS for C-flow so far have been confined to rather low values, no systematic Reynolds number effects on the mean values and turbulence characteristics have been investigated.

The objectives of the present paper are two-fold. The first is to study the effect of Reynolds number on the mean quantities and turbulence characteristics. Because the Reynolds number is a unique parameter for C-flow, we can obtain information on the effect of the Reynolds number on the channel flow that cannot be gained from P-flow study. The second objective is to make clear the characteristics of the large longitudinal vortices located in the central region of the channel along with their effects on the flow fields.

In § 2 a dimensional analysis is given to develop the similarity laws of mean and turbulence quantities. The experimental apparatus and method are presented in § 3, and discussion of the experimental results on mean velocity, turbulence statistics and longitudinal vorticies are given in § 4. Concluding remarks are given in § 5.

2. Similarity laws

Here, we develop similarity laws for mean velocity and turbulence intensity in order to discuss the effect of the Reynolds number on these variables. C-flow and P-flow are special cases of CP-flow. To derive the velocity similarity laws near the wall for C-flow and to discuss the laws in relation to those for P-flow, we first introduce the dimensional relations for $\partial U_1/\partial x_2$ of CP-flow, Nakabayashi *et al.* (2004):

$$\frac{\partial U_1^+}{\partial x_2^+} = f_1\left(\frac{x_2}{\delta_v}, \frac{h}{\delta_v}, \frac{\delta_s}{\delta_v}\right) = f_1(x_2^+, Re_*, \mu) \tag{1}$$

where U_1, x_2, and h are mean streamwise velocity, wall-normal distance and channel half-height, respectively. The superscript + indicates the wall variable normalized by the friction velocity u_* or δ_v. Here $\delta_v(= \nu/u_*)$ and $\delta_s(= \rho u_*^2/(\mathrm{d}\tau/\mathrm{d}x_2))$ are viscous and shear-stress-gradient length scales, respectively. ν is the kinematic viscosity.

$Re_*(= hu_*/\nu)$ is a Reynolds number based on u_* and h, and $\mu(= \rho u_*^3/(\nu \mathrm{d}\tau/\mathrm{d}x_2))$ is a shear-stress-gradient parameter. C-flow can be realized when $|\mu| \to \infty$ because $\mathrm{d}\tau/\mathrm{d}x_2 = 0$ and P-flow can be obtained when $\mu = -Re_*$, as is shown in figure 1. It can be said from this figure that as far as the μ-parameter is concerned, P-flow asymptotically approaches C-flow as Re_* increases. P-flow at low Re_*, however, has a clear difference with C-flow, because $|\mu|$ is small.

To obtain the mean velocity formula for the wall region, we integrate equation (1) with respect to x_2^+

$$U_1^+(x_2^+) = \int_0^{x_2^+} \frac{\partial U_1^+}{\partial x_2^+}\,\mathrm{d}x_2^+ = \int_0^{x_2^+} f_1(x_2^+, Re_*, \mu)\,\mathrm{d}x_2^+. \tag{2}$$

For U_1^+ in the fully turbulent region, the integration can be divided into two parts:

$$U_1^+(x_2^+) = \int_0^{x_{2b}^+} f_1(x_2^+, Re_*, \mu)\,\mathrm{d}x_2^+ + \int_{x_{2b}^+}^{x_2^+} f_1(x_2^+, Re_*, \mu)\,\mathrm{d}x_2^+. \tag{3}$$

Here, x_{2b}^+ indicates the distance to the boundary between the buffer and fully turbulent regions and has a value of about 70 for high-Re_* conventional wall turbulence, but a different value depending on Re_* and μ for low-Re_* or low-μ turbulent flow. This is because Re_* and μ effects penetrate into the wall region as the parameters decrease below certain values. The first term on the right-hand side shows the contribution from the viscous and buffer regions, while the second indicates that from the fully turbulent region. As is usual, the second term can be expressed using the Kármán constant κ:

$$\int_{x_{2b}^+}^{x_2^+} f_1(x_2^+, Re_*, \mu)\,\mathrm{d}x_2^+ = \int_{x_{2b}^+}^{x_2^+} \frac{1}{\kappa x_2^+}\,\mathrm{d}x_2^+ = \frac{1}{\kappa}\ln x_2^+ - \frac{1}{\kappa}\ln x_{2b}^+(Re_*, \mu). \tag{4}$$

As Nakabayashi *et al.* (2004) reported, κ has a constant value irrespective of Re_* and μ. Thus, the log law for CP-flow is

$$U_1^+(x_2^+) = \frac{1}{\kappa}\ln x_2^+ + B(Re_*, \mu) \tag{5}$$

where

$$B(Re_*, \mu) = \int_0^{x_{2b}^+} f_1(x_2^+, Re_*, \mu)\,\mathrm{d}x_2^+ - \frac{1}{\kappa}\ln x_{2b}^+(Re_*, \mu). \tag{6}$$

As the relation $\mu = -Re_*$ holds for P-flow, the log law can be expressed as

$$U_1^+ = \frac{1}{\kappa}\ln x_2^+ + B(Re_*, -Re_*). \tag{7}$$

The physical meaning of each Re_* in the parentheses of this relation is different. The first is the length scale ratio of h to ν/u_* indicating the effect of the outer scale on the wall region (conventional Re_* effect), while the second ($Re_* = -\mu$) is the shear stress gradient parameter. Equation (7) shows that the Re_* dependence of the U_1^+ profile for P-flow comes from a combination of Re_* and μ effects, although Re_* is apparently the only parameter for this flow. This indicates that variation of the P-flow profile with Re_* in the low-Re_* range does not necessarily mean that it is a low-Re_* effect on the law of the wall. For C-flow, however, due to $|\mu| \to \infty$, the μ parameter drops out from equation (5) and the velocity law can be written as

$$U_1^+ = \frac{1}{\kappa}\ln x_2^+ + B(Re_*). \tag{8}$$

Thus the Re_*-dependence of U_1^+ for C-flow, if any, shows the effect of Re_* itself on the law of the wall.

For the core region of C-flow, the velocity defect law can be given as

$$\frac{U_c - U_1}{u_*} = \frac{1}{1/Re_* + 2D_{1c}}\left(1 - \frac{x_2}{h}\right) = Rs(Re_*)\left(1 - \frac{x_2}{h}\right) \tag{9}$$

where U_c is the velocity at channel centre, Nakabayashi *et al.* (2004). Here, Rs is the slope of the defect law and generally a function of Re_*. $D_{1c}(= \nu_t/(2hu_*))$ is non-dimensinal eddy viscosity. Unlike P-flow, the defect law includes the Re_* effect due to the non-zero shear at the core region.

If x_{2u} is the distance to the boundary between the log law and the defect law, $x_{2u} = 0.2h$ is a good estimation for P-flow, Gad-el-Hak & Bandyopadhyay (1994), which is obtained from the assumption that the log law is valid in the range of constant Reynolds shear stress. For C-flow, however, Reynolds shear stress is inherently constant throughout the channel, and x_{2u} is obtained from different assumption and will have a value different from P-flow.

The turbulence intensity (r.m.s. value) of fluctuating velocity u_i', denoted as u_i, for C-flow can be expressed as

$$\frac{u_i}{u_*} = f_2(x_2^+, Re_*). \tag{10}$$

A linear relation can be expected for a very small x_2^+ range as

$$\frac{u_i}{u_*} = A_1 x_2^+. \tag{11}$$

There exists a region far but not too far from the wall where the inner and outer scales δ_v and h do not have a significant effect on turbulence. Thus, x_2^+ and Re_* should be dropped from f_2 in this region, and the turbulence intensity has a constant value, i.e. plateau region:

$$\frac{u_i}{u_*} = C_i \tag{12}$$

Further away from the wall, i.e. in the core region, u_* and h are typical scales for turbulence and the following similarity law holds (the parameter Re_* is included for the same reason as in equation (9)):

$$\frac{u_i}{u_*} = f_3\left(\frac{x_2^+}{h}, Re_*\right). \tag{13}$$

3. Experimental apparatus and method

Figure 2 shows a schematic diagram of the experimental setup for C-flow. The test channel consists of a stationary wall on one side and a moving wall on the other, and is 5.12 m in length and 0.88 m in width. The channel height $2h$ was selected as 27 mm, except when the Reynolds number Re $(= hU_b/(2\nu)$, U_b is moving wall velocity$) = 5000$, for which 47 mm was adopted. The moving wall consists of a conveyer belt made of polyurethane. The tension of the belt was carefully adjusted by two rollers so as to run smoothly on the base plate without any fluttering and/or sinuous motion. The coordinate system is (x_1, x_2, x_3), where x_1, x_2 and x_3 are the streamwise distance from the centreline of the forward roller, the wall-normal distance from the stationary wall and the spanwise distance from the centre line of the channel, respectively.

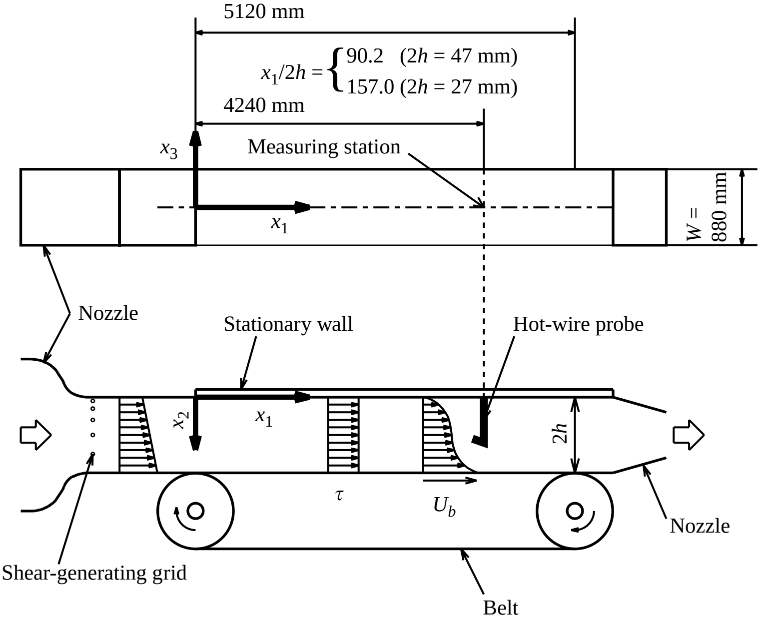

FIGURE 2. Experimental apparatus.

The air was blown through a two-dimensional nozzle into the channel inlet section, where a shear-generating grid was installed to promote fully developed C-flow in a short inlet length. The grid was designed based on the theory of McCarthy (1964) to generate a mean shear rate of $(2h/U_b)\,\mathrm{d}U_1/\mathrm{d}x_2 = 0.38$ in the central part of the channel. To minimize the effect from various disturbances in the laboratory on the C-flow, the nozzle was installed at the channel exit.

The instantaneous velocity of the C-flow was measured by a hot-wire anemometer using I- and X-type probes. The I-probe utilized 5 μm tungsten wire with 0.8 mm sensing length, whereas the two X-probes, u_1u_2 and u_1u_3, used 3 μm tungsten wire with 0.5 mm sensing length. The separation between the two wires of the X-probe was 0.5 mm. The signals from the hot-wire anemometer were stored on a PC disk through a 12-bit A/D converter with a sampling rate of 10 kHz for 120 s. The distance of the wire closest to the stationary wall was measured by viewing the wire and its reflection image on the wall in a microscope within an accuracy of ±0.003 mm. The pressure holes, 0.8 mm in diameter, were placed on the stationary wall, every 500 mm in the x_1-direction, and the wall static pressure was measured by a precision pressure cell having 0.1 Pa resolution. Belt speed U_b was measured optically by counting the number of tape strips glued on the belt as they passed a photo detector in a unit of time.

Friction velocity u_* was estimated from the mean velocity near the stationary wall measured by the I-probe, based on the principle proposed by Bhatia, Durst & Jovanovic (1982) and on the procedure used by Nagano, Tagawa & Tsuji (1991). According to Bhatia *et al.* the apparent nominal velocity profile close to the wall

$$U^+ = F(x_2^+) \tag{14}$$

is identical as long as the probe and materials of the wall and wire are the same.

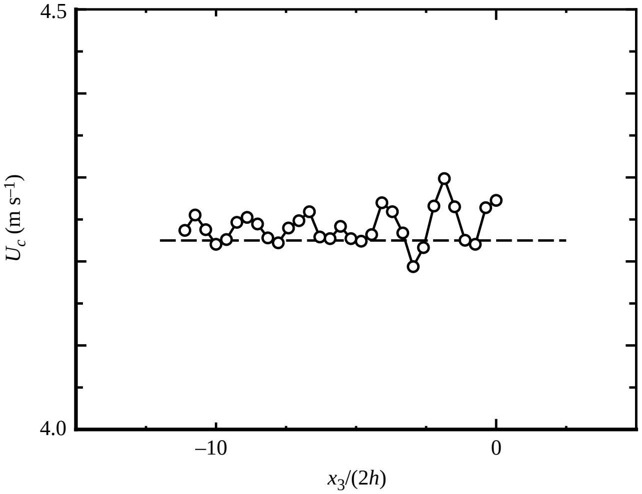

FIGURE 3. Spanwise variation of U_c at $x_1/(2h) = 157$ for $Re_* = 192$. Broken line shows $U_b/2$.

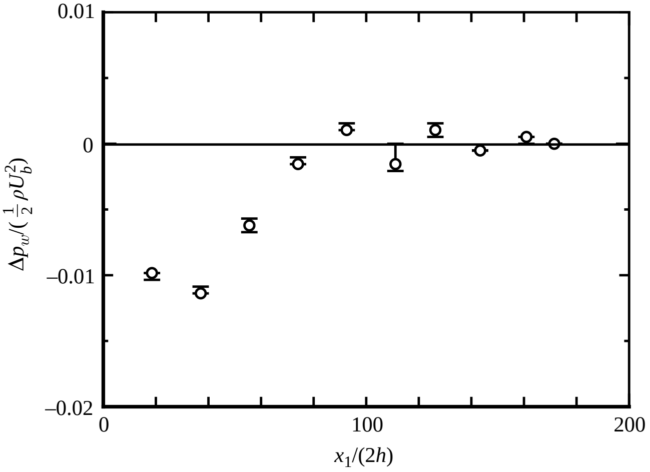

FIGURE 4. Wall pressure distribution along the streamwise direction at $Re = 3750$.

For a given moving wall speed U_b, C-flow was developed by adjusting the flow rate into the channel so that the following two conditions were satisfied. First, that the pressure gradient along x_1 is zero, and second, that mean velocity at the channel centre, $x_2 = h$, $\langle U_c \rangle$ is set equal to $U_b/2$ within a 1 % margin of error at the measuring station. Here, we use the value averaged along the spanwise direction, indicated by bracket $\langle \cdot \rangle$, because U_c varies sinuously along the x_3-direction in C-flow, as is shown in figure 3. Figure 4 shows a typical example of wall pressure distribution $\Delta p_w = p_w - p_r$ at $Re = 3750$, where p_r is reference wall pressure at $x_1/(2h) = 171$. In the downstream section of $x_1/(2h) \geqslant 90$, the wall pressure is almost constant within ± 0.1 % of $\frac{1}{2}\rho U_b^2$, and C-flow is expected to be fully developed there. At very low Reynolds numbers, however, the wall pressure method does not work well because Δp_w is so small that the resolution of the pressure cell is not sufficient to obtain convincing data, and recourse is made to the second condition noted above. The development of the velocity distribution from the inlet section was carefully studied to obtain a fully

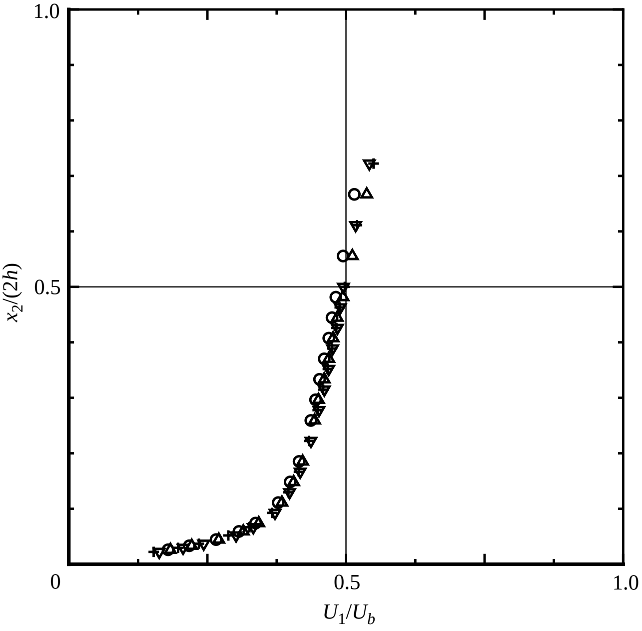

FIGURE 5. Development of mean velocity distribution at $Re = 3750$. $x_1/(2h)$: +, 40; △, 72; ▽, 106; ○, 157.

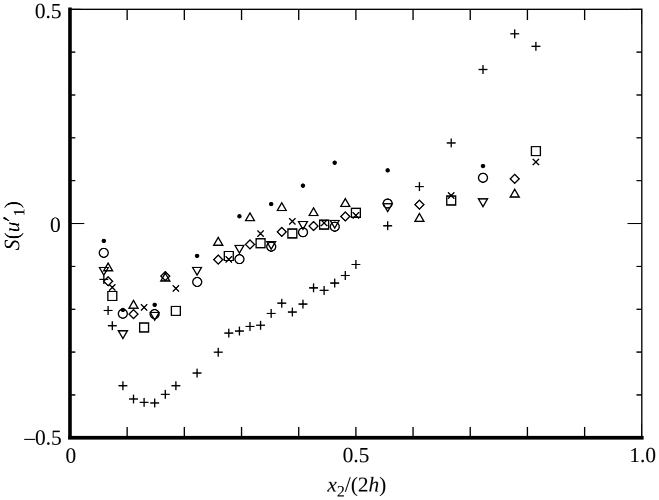

FIGURE 6. Development of skewness factor distribution at $Re = 3750$. $x_1/(2h)$: +, 40; ●, 55; △, 72; □, 89; ▽, 106; ◇, 123; ×, 140; ○, 157.

developed C-flow. Figures 5 and 6 show the development of the mean velocity U_1 and skewness $S(u'_1)$ along $x_1/(2h)$ at $Re = 3750$. Although U_1 is apparently fully developed at $x_1/(2h) = 40$, the skewness $S(u'_1)$, one of the higher turbulence moments, requires a longer inlet length of $x_1/(2h) = 72$–89 to confirm full development. This result is consistent with that of the wall pressure. In this work, the test section was placed at $x_1/(2h) = 157$ for the $2h = 27$ mm channel or $x_1/(2h) = 90$ for the $2h = 47$ mm channel.

	$Re_* = (hu_*/\nu)$	$Re = (hU_b/2\nu)$	Symbol
Couette flow	253	5000	○
	192	3750	△
	138	2500	□
	100	1750	▽
	73	1250	◇
	50	750	◎
Poiseuille flow	191	3750	▲
	97	1750	▼

TABLE 1. Experimental conditions and symbols.

Under ideal conditions, i.e. having no preferred position along the spanwise direction, the long-time-averaged velocity U_c is considered to have no wavy pattern along the x_3-direction. In the physical experiment on C-flow, however, the uncontrollable small disturbance and/or finite width of the channel could induce a wavy pattern in the velocity profile as shown in figure 3. The wavy pattern was also confirmed by Pitot tube measurements. The Pitot tube system had a time constant of one minute and a long time average was possible. The wavy variation, however, is less than about ± 1 % in the present experiment. This spanwise variation of U_c is due to the existence of large-scale streamwise vortices, as was indicated by Lee & Kim (1991) in their DNS. Because the large-scale streamwise vortices were quasi-stationary in their DNS, the variation of U_c was anomalously large, about ± 20 %. However, since the large-scale streamwise vortices are not stationary in space and time as Komminaho *et al.* (1996) pointed out, the wavy pattern of U_c would be blurred, although it would not completely disappear, as shown in figure 3. Considering that the the spanwise variation of U_c is small and the associated u_* variation almost cancels the U_1 variation if expressed in wall variable like U_1/u_*, we can disregard the spanwise variation of U_1 as well as the turbulence quantities in the first part of this work (§ 4.1 to § 4.3); thus, the measurements were made at $x_3 = 0$. In discussing the characteristics and the effect of the large-scale streamwise vortices on the flow fields (§ 4.4), the spanwise variation of the velocity profile was also measured.

The experiments were performed under six conditions for C-flow and two conditions for P-flow, as summarized in table 1, where the Reynolds numbers, $Re_* = hu_*/\nu$ and $Re = hU_b/(2\nu)$, and the corresponding symbols are given. The P-flows were realized in the same channel by making the belt stationary.

4. Experimental results and discussions

4.1. *Wall friction coefficient*

The wall friction coefficient C_f, defined based on $U_c(= U_b/2$ for C-flow) as

$$C_f = \frac{\tau_w}{\frac{1}{2}\rho U_c^2}, \tag{15}$$

is compared with other researcher's results, including results for P-flow and C-flow from the physical experiment and DNS, in figure 7. Here, τ_w is the wall shear stress. Since the transitional Reynolds number of C-flow from laminar to turbulent flow was reported as $(Re)_t = 360$ by Tillmark & Alfredsson (1992), the lowest Reynolds number in the present study, $Re = 750$, is well within that for a fully developed turbulent

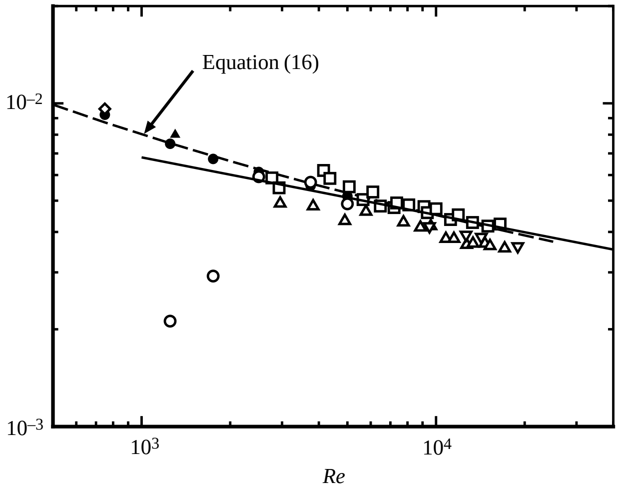

FIGURE 7. Wall friction coefficient C_f. Experiment: ●, present; ○, Nakabayashi *et al.* (1988); △, Reichardt; □, Robertson & Johnson; ▽, El Telbany & Reynolds (1982). DNS: ◇, Komminaho *et al.*; ▲, Bech *et al.* Empirical formulae: – – – –, Robertson & Johnson for C-flow; ——, Hussain & Reynolds for P-flow.

C-flow. The present results show fairly good agreement with those of Robertson & Johnson (1970) and DNS by Bech *et al.* (1995) and Komminaho *et al.* (1996). The empirical formula proposed by Robertson & Johnson

$$C_f = \frac{0.0722}{(\log Re)^2}, \tag{16}$$

shown by a broken line in the figure, is a good estimation for C_f in the range of $750 \leqslant Re \leqslant 16500$. The results of Reichardt (1959) and El Telbany & Reynolds (1982) are slightly lower. Nakabayashi *et al.* (1988) reported that the experimental results of El Telbany & Reynolds suffered from a short inlet length resulting in a lower turbulent intensity, which may have caused a lower C_f in their results. The results of Nakabayashi *et al.* (1988) are anomalously low in the range of $1000 < Re < 2000$. An adjustable plate normal to the flow instead of the shear generating grid was installed at the exit of the two-dimensional nozzle in their experiment. The transitional Reynolds number to turbulent flow might be delayed in their experiment due to the different channel inlet condition.

The solid line, the empirical formula of C_f for P-flow reported by Hussain & Reynolds (1975), has almost the same value as equation (16) in the range of $Re \geqslant 4000$. Because of the relation $C_f = 2/(U_c^+)^2$, where $U_c^+ = U_1(h)/u_*$, this suggests that the mean velocity profile on one side of a wall normalized by friction velocity, U_1^+, is almost the same for the two flows, except for the low Reynolds number range. At low *Re*, less than 4000, C_f of C-flow is larger than that of P-flow. This indicates that there exists some difference in the velocity profile and/or the turbulence characteristics between C- and P-flows in this low-Reynolds-number range.

4.2. *Mean velocity profile*

To study the mean velocity profile in detail, we first consider the flow region diagram for C-flow. The mean flow velocity profile can be divided into linear, buffer, log and defect regions, respectively. To this end, the variations of $x_2^+ \mathrm{d}U_1^+/\mathrm{d}x_2^+$ against x_2^+ are

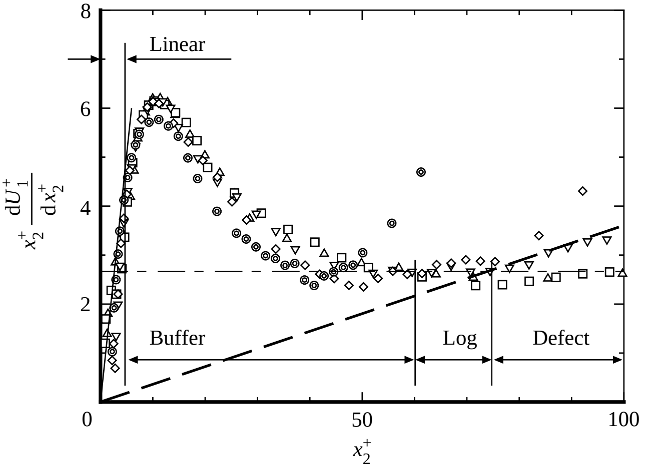

FIGURE 8. Distribution of $x_2^+\,dU_1^+/dx_2^+$. For symbols, see table 1. Fitting lines for $Re_* = 100$: ——, linear region; —–—, log region; – – – –, defect law region.

studied as in figure 8, where each region has the following relation:

$$x_2^+ \frac{dU_1^+}{dx_2^+} = x_2^+ \qquad \text{linear region,}$$

$$x_2^+ \frac{dU_1^+}{dx_2^+} = \frac{1}{\kappa} \qquad \text{log law region}$$

$$x_2^+ \frac{dU_1^+}{dx_2^+} = \frac{Rs}{Re_*} x_2^+ \qquad \text{defect law region.}$$

Each of the three lines drawn to fit the experimental data for $Re_* = 100$ in the figure corresponds to one of the above relations. From these fitting lines and the corresponding data points, we can estimate the range of each region, as shown in the figure. The flow regions thus obtained for various Re_* are summarized as a flow region diagram in figure 9.

In the linear region $0 \leqslant x_2^+ \leqslant 5$, an Re_* effect cannot be seen. A buffer region exists between the linear and log regions. The boundary between the buffer and log regions, denoted by x_{2b}^+ and indicated by a bold broken line, is Re_*-independent and is located around 80 when Re_* is greater than 200. However, it shifts toward the wall as Re_* decreases below around 150. This indicates that the low-Re_* effect in the buffer region appears when $Re_* < 150$. The mechanism of this low-Re_* effect is not yet known, but the penetration of strong ejection from the opposite wall may be a possible cause. The upper boundary of the log law (or lower boundary of defect law), denoted as x_{2u}^+, is indicated by a fine broken line in the figure. This can also be given as a crossing point between the log and defect laws like $x_{2u}^+ = Re_*/(\kappa Rs)$. Taking $Rs \sim 3$ as given later, $x_{2u}^+ \sim 0.8\,Re_*$. Comparison of this with $x_{2u}^+ = 0.2\,Re_*$ for P-flow reveals that the log-law area in C-flow is significantly wider than that in P-flow. The two boundaries x_{2b}^+ and x_{2u}^+ merge when Re_* is about 50–70, which is considered to be the lowest Re_* for the existence of a log region. Due to the scatter of data and difficulty of fitting them on a line in figure 8 at such low Re_*, the existence of the log law is not so certain in the range $Re_* < 100$. Therefore, the boundary lines of x_{2b}^+ and x_{2u}^+ shown in figure 9 are indicated by dotted lines instead of broken lines in this range. As shown

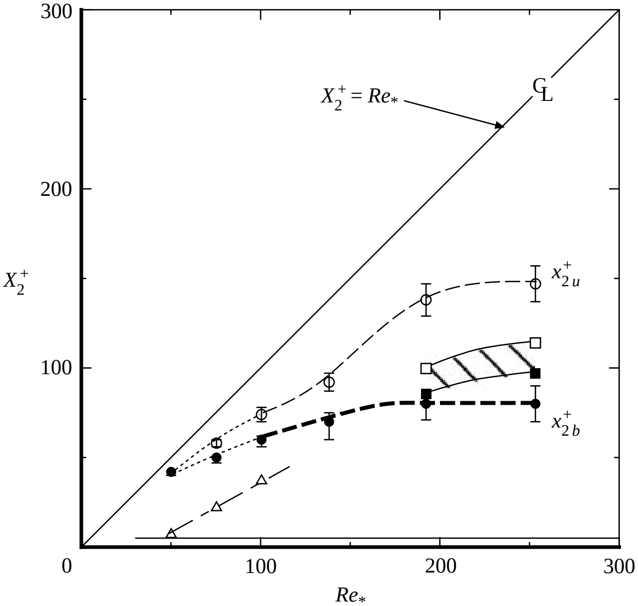

Figure 9. Flow region diagram: ——, outer boundary of linear region; – – –, boundary between buffer and log regions; ————, boundary between log and defect regions; —·—, penetration depth of Re_* effect in buffer region; /////, plateau region of u_1^+.

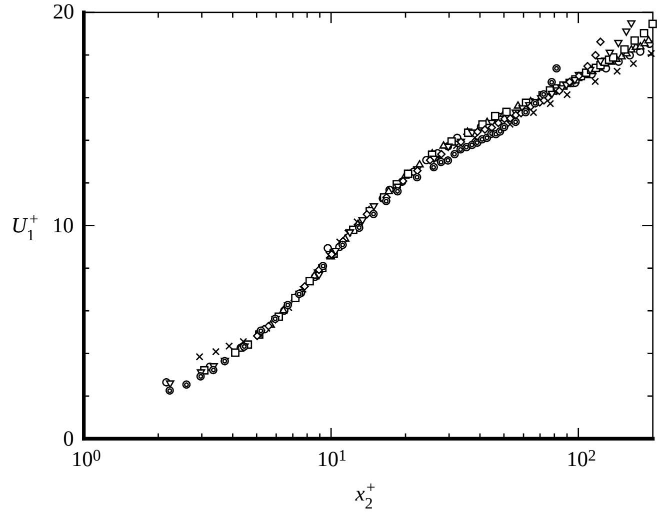

Figure 10. Wall law of Couette flow. For symbols, see table 1. ×, Poiseuille flow by Hussain & Reynolds at $Re = 55200$.

later, Rs increases with Re_*, and the ratio of width of the defect law $h_D(= h - x_{2u})$ to half the channel height, $h_D/h = (1 - 1/(\kappa Rs))$, increases with Re_*.

Figure 10 shows the mean velocity profiles plotted in wall variables on a semi-log graph for various Reynolds numbers. The P-flow data of Hussain & Reynolds (1975) are also given in the figure for comparison. All present data follow the log law, equation (8). Applying the least square fit to the data of the corresponding area, the

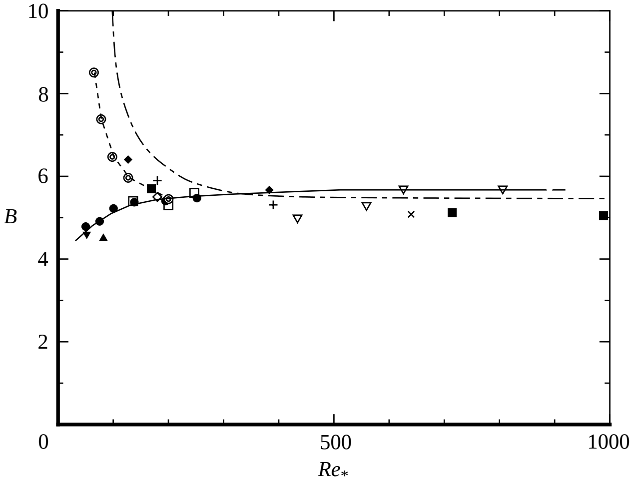

FIGURE 11. Variation of additive constant B with Re_*. Couette flow: ●, present; □, Nakabayashi *et al.* (1988); ▽, El Telbany & Reynolds (1980); ▲, Bech *et al.*; ▼, Komminaho *et al.*; ——, most probable curve for Couette flow. Poiseuille flow: ◎, Patel & Head; ■, Wei & Willmarth; ◆, Nakabayashi *et al.* (1995); +, Antonia *et al.*; ×, Hussain & Reynolds; ◇, Kim *et al.*; – – – –, fitting curve for channel; —–—, pipe flow.

Kármán constant κ is shown to be a constant of 0.4 irrespective of the Reynolds number. However, the additive constant B changes slightly with Re_*. The Reynolds number dependence of B is shown in figure 11, in which the results for P-flow in a parallel plate and pipe reported by Patel & Head (1969) are given by broken and chain-dot lines, respectively. The general trend of P-flow is that B increases as Re_* decreases below around 300. For C-flow, however, B decreases from 5.5–5.7 at its high-Reynolds-number value, as Re_* decreases below around 150. There is a large difference between the two flows. It is generally believed that the flow near the wall is similar for both C- and P-flows, Lee & Kim (1991). This is true for high-Reynolds-number flows, but not for low-Reynolds-numbers. This can be explained as follows. As developed in §2, B depends only on Re_* for C-flow but depends on Re_* and implicitly on μ for P-flow, see equations (7) and (8). As a consequence, reduction of B with Re_* for C-flow is the effect of low Reynolds number. The increase of B for P-flow is caused by the effect of μ rather than that of Re_*, which has been confirmed by Kitoh, Nakabayashi & Kotoh (1995).

The low-Reynolds-number effect on B for C-flow can be explained by the change of x_{2b}^+ and/or that of U_1^+ profile in the buffer region with Re_*, as developed in equation (6). As already shown in figure 9, x_{2b}^+ decreases with Re_* if Re_* is smaller than about 150. The subtle change in the U_1^+ profile can be studied more easily through the distribution of $x_2^+ \mathrm{d}U_1^+/\mathrm{d}x_2^+$. If Re_* is larger than around 150 the distributions of $x_2^+ \mathrm{d}U_1^+/\mathrm{d}x_2^+$ collapse on a single curve in the buffer region but shift downward for Re_* less than 150. The chain dot line in figure 9 indicates the boundary in the buffer region above which the U_1^+ profile is affected by Re_*. The effect of Re_* penetrates into smaller x_2^+ as Re_* decreases. The combined effects of variations of the x_{2b}^+ and U_1^+ profile in the buffer region are responsible for the decrease of B at low Reynolds numbers.

From the variation of B with Re_*, the critical Reynolds number at which the law of the wall for U_1^+ begins to be affected is $Re_* = 150$–200. Below this Reynolds number,

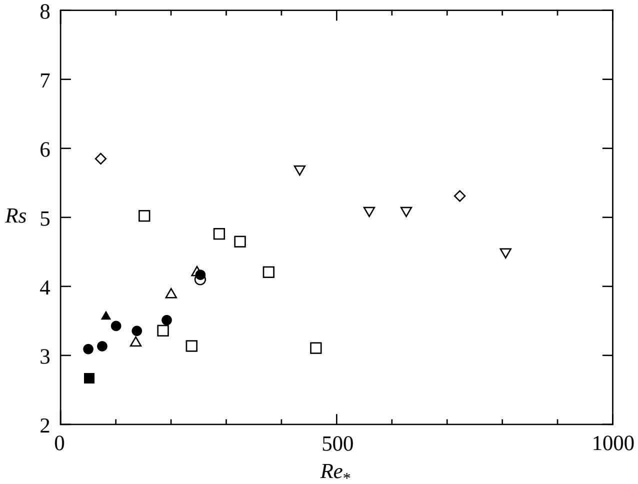

FIGURE 12. Variation of R_s with Re_*. Experiment: ●, present; □, Robertson & Johnson; ▽, El Telbany & Reynolds (1982); ○, Nakabayashi *et al.* (1994); △, Nakabayashi *et al.* (1988); ◇, Reichardt. DNS: ▲, Bech *et al.*; ■, Komminaho *et al.*

the buffer region is forced to contract as Re_* decreases. This is the reverse of the trend for P-flow.

In the velocity defect law, equation (9), $Rs = (\partial U_1/\partial x_2)(h/u_*)$ is the slope of the defect law that indicates the ratio of a typical large turbulence time scale (h/u_*) to the mean shear time scale $(\partial U_1/\partial x_2)^{-1}$. Rs varies with Re_*. The variation of Rs with Re_* is summarized in figure 12 together with other researchers' results. The present results and DNS strongly support the increasing trend of Rs in the range of $Re_* \leqslant 250$, while the results of Robertson & Johnson (1970) show the reverse trend. Equation (9) shows that the increase in Rs in the low-Re_* region is partly due to a direct viscous effect but mostly due to the change of D_{1c} with Re_*. At higher Re_*, $Re_* \geqslant 500$, Rs seems to approach a constant value of about 5, but lack of reliable data prevented us from making a decisive conclusion.

4.3. *Turbulence characteristics*

Figure 13 shows the distribution of the turbulent kinetic energy production Pr^+ against x_2^+. Pr^+ for CP-flow can be given as

$$Pr^+ = -\overline{u_1'^+ u_2'^+}\frac{\mathrm{d}U_1^+}{\mathrm{d}x_2^+} = \left(1 + \frac{x_2^+}{\mu}\right)\frac{\mathrm{d}U_1^+}{\mathrm{d}x_2^+} - \left(\frac{\mathrm{d}U_1^+}{\mathrm{d}x_2^+}\right)^2. \tag{17}$$

For P-flow there is an explicit effect of μ, as is given in the above equation (conventionally, this effect is described as the Re_*-effect). An appreciable Pr^+-distribution change with Re_* has been reported by Antonia *et al.* (1992). For C-flow, however, because the $|\mu| \rightarrow \infty$, the Pr^+-profile seems to be universal and no explicit Reynolds number effect can be expected. The experimental results also confirm that there is no noticeable Reynolds number effect, and that the profile is quite similar to that of P-flow at high Reynolds numbers. Komminaho *et al.* (1996) discussed in their paper that the Pr^+-profile of C-flow is the high-Reynolds-number equivalent of P-flow, the maximum value of which is 0.25 at $\mathrm{d}U_1^+/\mathrm{d}x_2^+ = 0.5$ (at x_2^+ is about 12). For very low Reynolds numbers, however, the implicit effect of Re_* on the Pr^+-profile appears through the variation of the velocity profile, $U_1^+(x_2^+)$, with Re_*. For Re_* less than

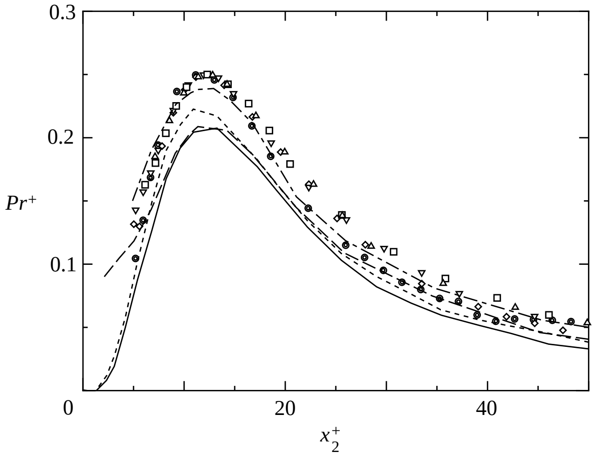

FIGURE 13. Production of kinetic energy of turbulence. For symbols, see table 1. Poiseuille flow: ——, Antonia *et al.* ($Re = 3300$); ----, Antonia *et al.* ($Re = 7900$); ———, Wei & Willmarth ($Re_* = 169$); —-—, Wei & Willmarth ($Re_* = 717$).

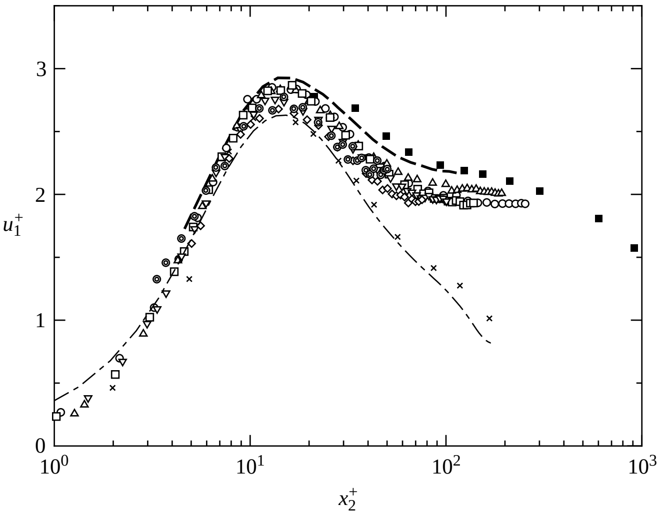

FIGURE 14. Turbulence intensity profile $u_1{}^+$. For symbols, see table 1. Couette flow: ———, Lee & Kim ($Re_* = 170$). Poiseuille flow: ×, Wei & Willmarth ($Re_* = 169$); ■, Wei & Willmarth ($Re_* = 1608$); —-—, Kim *et al.* ($Re_* = 180$).

about 100, Pr^+ has a lower value than the high-Re_* value in the area $x_2^+ > 18$ for $Re_* = 50$ and $x_2^+ > 35$ for $Re_* = 73$. This shows that the influence of low Reynolds numbers on the turbulent energy production appears in the buffer region.

Figure 14 shows the turbulence intensity distribution normalized by the friction velocity, $u_1^+ = (\overline{u_1'^2})^{1/2}/u_*$. For C-flow, the change of the distribution with the Reynolds number is quite small compared with that for P-flow reported by many researchers, Wei & Willmarth (1989) for example. Up to $x_2^+ \risingdotseq 6$, the linear relation of equation (11) with a coefficient $A_1 = 0.33$ holds and no Reynolds number effect can be seen there. In the buffer region, $8 \leqslant x_2^+ \leqslant 80$–$90$, an Re_* effect on the profile can be seen

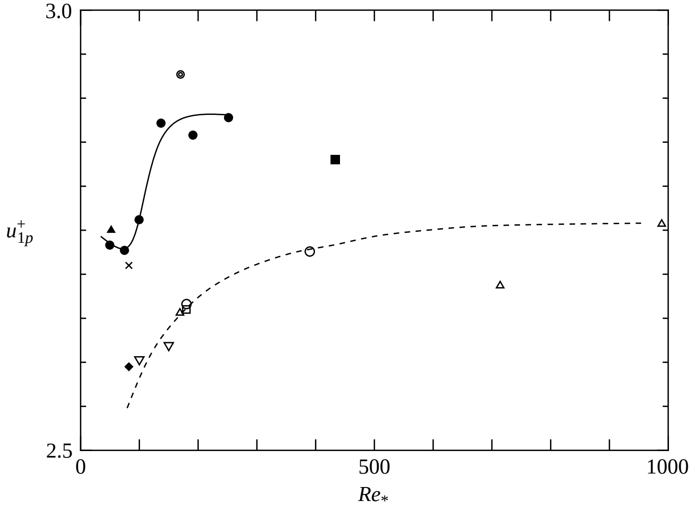

FIGURE 15. Variation of peak value of $u_1{}^+$ with Re_*. Couette flow: ●, present; ◎, Lee & Kim; ×, Bech *et al.* (DNS); ◆, Bech *et al.* (Exp.); ▲, Komminaho *et al.*; ■, El Telbany & Reynolds (1982); ——, fitting curve for C-flow. Poiseuille flow: ○, Antonia *et al.*; △, Wei & Willmarth; ▽, Kuroda; - - - -, fitting curve for P-flow.

for low Re_*, and u_1^+ decreases as Re_* decreases. The decrease of Pr^+ at low Re_* is one reason for the low u_1^+.

In the central area, the core region exists where an outer length scale h dominates, as shown by equation (13). From the experimental results, u_1^+ is constant at about 2. At first glance, the constant-valued core region extends down to the edge of the buffer region, $x_2^+ \sim 80$. However, a closer look at the profile, not shown here, reveals a small area with a different constant between the buffer and core regions; it is slightly higher (~ 0.07) than that in the core region. This area could correspond to the plateau region introduced in equation (12). This plateau region is indicted by a hatched area in the flow region diagram, figure 9. The area is completely embedded in the log region. It is interesting to note that P-flow in a pipe has a similar plateau region. From careful measurements of pipe flow, Perry & Abell (1975) obtained the constant value area $u_1^+ \fallingdotseq 2.1$, whose region is consistent with the log law.

The peak value of u_1^+, denoted as u_{1p}^+, is located at $x_2^+ \fallingdotseq 14$. The variations of u_{1p}^+ for C- and P-flows with Re_* are summarized in figure 15. C-flow has a constant value of $u_{1p}^+ \fallingdotseq 2.88$ when $Re_* \geqslant 150$ but shows a sharp drop to about 2.72 for a small Re_* change. For P-flow, u_{1p}^+ increases gradually with Re_*, which may be due to the μ-effect on Pr^+. This P-flow trend is also confirmed in the review article by Gad-el-Hak & Bandyopadhyay (1994).

Turbulence intensity of the wall-normal component u_2^+ is shown in figure 16. The present data are limited to the range $x_2^+ \geqslant 40$ because of wall interference with the hot-wire probe. No Re_* effect can be seen. In the range $x_2^+ \geqslant 70$, u_2^+ has a constant value of 1.16. The profile of P-flow largely depends on Re_* and asymptotically approaches the C-flow profile as Re_* increases.

The skewness $S(u_1')$ and flatness $F(u_1')$ are shown and compared with the P-flow in figures 17 and 18. The present data are consistent with the DNS result of Bech *et al.* (1995). No difference in the $S(u_1')$ profile between C-flow and P-flow can be seen close to the wall, $x_2^+ \leqslant 12$. In the buffer region, $S(u_1')$ takes on typical negative values

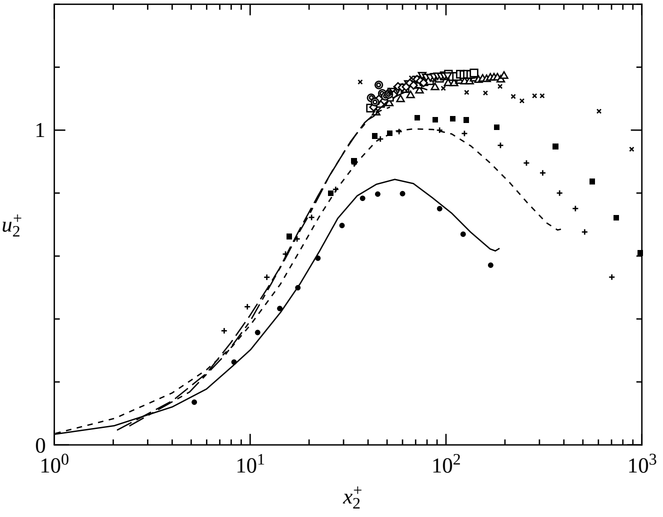

FIGURE 16. Turbulence intensity profile $u_2{}^+$. For symbols, see table 1. ———, DNS by Bech *et al.* for Couette flow ($Re_* = 82$). Re_* for Poiseuille flow by Wei & Willmarth: ●, 169; +, 714; ■, 989; ×, 1608. DNS by Antonia *et al.*: ——, $Re = 3300$; - - - -, $Re = 7900$.

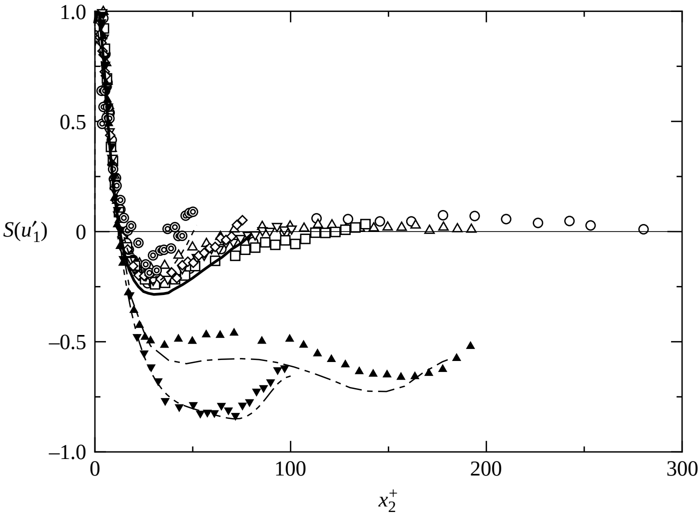

FIGURE 17. Skewness factor of u'_1. For symbols, see table 1. ——, DNS by Bech *et al.* for Couette flow ($Re_* = 82$). Poiseuille flow: ▲, present ($Re_* = 191$); ▼, present ($Re_* = 97$); —-—, DNS by Kim *et al.* ($Re_* = 180$); —- -—, DNS by Kuroda ($Re_* = 100$).

of wall turbulence showing a distinctive ejection motion. However, $|S(u'_1)|$ of C-flow is smaller than that of P-flow, which means that the ejection for C-flow is relatively less important than that for P-flow. In the fully turbulent region, $x_2^+ \geqslant 70$, $S(u'_1) \risingdotseq 0$, compared with the large negative value for P-flow. C-flow has non-zero Pr^+ even in the central area, and the turbulence activity there is fairly strong compared with that in the P-flow that brings an intensified sweep motion down in the wall direction. This is why $|\ S(u'_1)\ |$ becomes low in C-flow. $F(u'_1)$ has the same features as $S(u'_1)$. Up to $x_2^+ \sim 12$, both C- and P-flows show a typical wall turbulence profile, i.e. high value

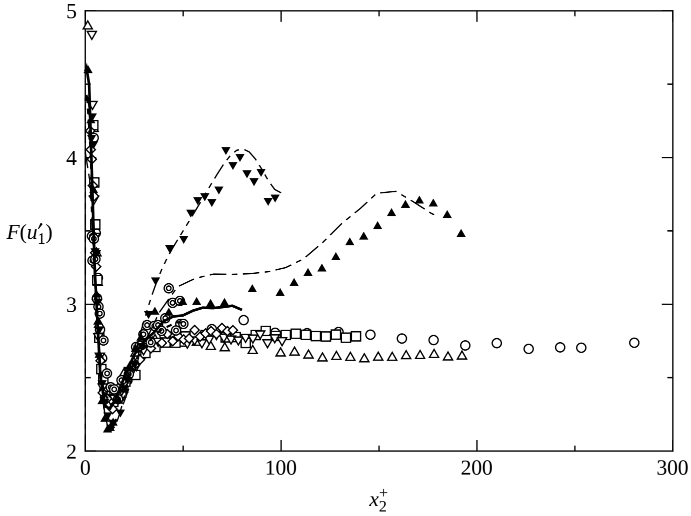

FIGURE 18. Flatness factor of u'_1. For legend, see figure 17.

very close to the wall followed by a sharp drop to its minimum at about $x_2^+ \sim 10$ after which it increases again. At $x_2^+ \geqslant 40$, C-flow has a constant value of 2.7–2.8, while the P-flow has a higher value and the profile varies with Re_*. Judging from the $S(u'_1)$ and $F(u'_1)$ profiles, it is only very close to the wall region ($x_2^+ \leqslant 12$) that C-flow has conventional wall turbulence properties. Away from that region, the enhanced sweep motion makes the C-flow turbulence different from that in P-flow. The probability density of u'_1 has a more Gaussian-like character, especially in the fully turbulent region.

The generation of the Reynolds shear stress in C-flow is examined by a joint probability density distribution of u'_1 and u'_2. Figure 19 shows the distribution at $x_2^+ = 40$. The P-flow result is also shown for comparison. On the negative-u'_1 side, C-flow and P-flow have the same distribution, whereas on the positive-u'_1 side the distribution of C-flow extends to a higher u'_1 than in P-flow. The Reynolds shear stress in C-flow is generated more evenly by both ejection and sweep. This indicates that it is not the ejection ($u'_1 < 0$) but the sweep ($u'_1 > 0$) coming from the central area that characterizes C-flow turbulence.

Figure 20 shows the correlation coefficient $R_{12}(= -\overline{u'_1 u'_2}/(u_1 u_2))$. Except for the wall vicinity, R_{12} has a nearly constant value of about 0.43, which is fairly close to that of the uniform shear flow $R_{12} = 0.45$–0.47 reported by Tavoularis & Karnik (1989). The anomalous results $R_{12} = 0.7$ of El Telbanny & Reynolds (1982) are due to the short inlet length needed to obtain developed C-flow.

Figure 21 shows the auto-correlation coefficient $R_{11}(\tau)$ of $u'_1(t)$. Here τ is the time separation. Using Taylor's frozen turbulence hypothesis, $R_{11}(\tau)$ can be translated into a two-point velocity correlation coefficient $R_{11}(\Delta x_1)$. It is generally accepted that C-flow has a long correlation time (or length) compared to P-flow. At the channel centre, the time separation τ at which $R_{11}(\tau)$ crosses zero is $40h/U_b$, irrespective of the Reynolds number, which is about 3 times as long as that of the P-flow at $Re_* = 191$. In the figure, the DNS results of Komminaho *et al.* (1996) and the experiment by Tillmark & Alfredsson (1994), are shown for comparison. All results, except for Tillmark & Alfredsson's (1994) with $Re = 3360$, coincide in the range $\Delta x_1/h \leqslant 10$, but the DNS

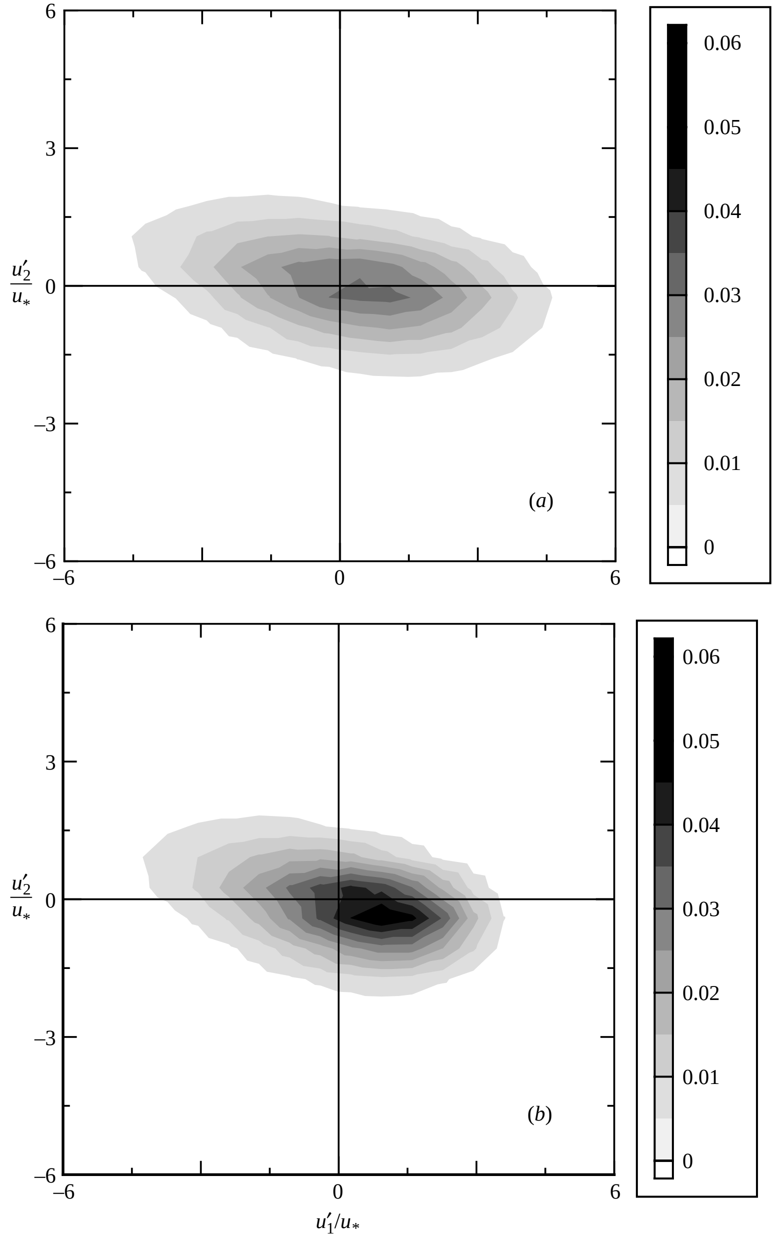

FIGURE 19. Joint probability density of u'_1 and u'_2 at $x_2{}^+ = 40$. (*a*) Couette flow at $Re_* = 192$. (*b*) Poiseuille flow at $Re_* = 191$.

result has a stronger correlation than the present one at greater distances. As Komminaho *et al.* admitted in their paper, $R_{11}(\Delta x_1)$ was overpredicted due to the self-imposed symmetry constraint, and R_{11} had a non-zero value even at $\Delta x_1 = 44h$. They also showed a streaky structure of streamwise velocity with the associated vorticity, which is the reason for the long correlation length of R_{11}. Tillmark & Alfredsson (1994) found a larger correlation at $Re = 3360$ than that at $Re = 1240$, and concluded that the structures are more pronounced at high Re. However, compared

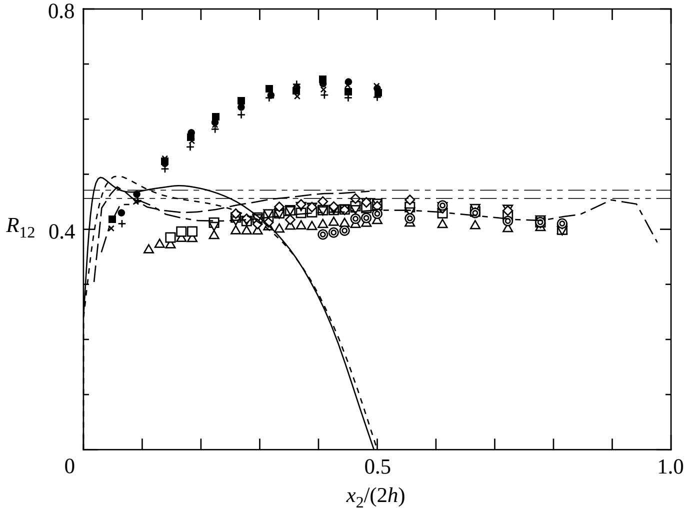

FIGURE 20. Correlation coefficient R_{12} between u'_1 and u'_2. For symbols, see table 1. Re_* of Couette flow of experiment by El Telbany & Reynolds (1982): ●, 434; ■, 560, +, 626; ×, 806. DNS of Couette flow: — — — —, Bech *et al.* ($Re_* = 82$); —–—, Komminaho *et al.* ($Re_* = 52$). DNS of Poiseuill flow: ——, Kim *et al.* ($Re_* = 180$); - - - -, Kuroda ($Re_* = 100$). —·—·—, uniform shear flow by Tavoularis & Karnick.

with the present result having a similar Reynolds number of 3750, *Re* is indeed not a defining parameter for the structures. Perhaps the channel geometry and/or inlet condition may have some effect on the structures. Close to the wall ($x_2^+ = 15$), the correlation length is decreased in C-flow, but is still longer than in P-flow, whose integral length scale is known to become larger as the wall is approached.

4.4. *Large longitudinal vortical structure*

The streamwise velocity component U_1 has a distinct quasi-periodic change along the spanwise direction, as was described in § 3. We introduce a mean velocity, $\langle U_1 \rangle$, averaged in the spanwise direction and the wavy component $\tilde{u}_1$ as

$$\left.\begin{aligned} \langle U_1(x_1, x_2) \rangle &= \frac{1}{L} \int_{-L/2}^{L/2} U_1(x_1, x_2, x_3)\, \mathrm{d}x_3, \\ \tilde{u}_1(x_1, x_2, x_3) &= U_1(x_1, x_2, x_3) - \langle U_1(x_1, x_2) \rangle. \end{aligned}\right\} \tag{18}$$

Here, L is a spanwise length long enough to obtain an appropriate average, or one wavelength in the case of periodic variation. The instantaneous velocity U_1 is decomposed into $\langle U_1 \rangle$, $\tilde{u}_1$ and the fluctuating component u'_1 as

$$U_1(x_1, x_2, x_3, t) = \langle U_1(x_1, x_2) \rangle + \tilde{u}_1(x_1, x_2, x_3) + u'_1(x_1, x_2, x_3, t). \tag{19}$$

The wavy pattern of $\tilde{u}_1$ and its amplitude depend on the inlet conditions to the channel, e.g. the type of shear-generating grid, but never disappear in any way. This wavy variation is caused by large longitudinal vortical structures, as was indicated by Lee & Kim (1991). Considering the work by Komminaho *et al.* (1996) that showed the vortical structures are neither stationary in time nor space, it is conjectured that the vortical structures fluctuate around their average position. The velocity measured at a fixed point may fluctuate due to the vortical structure fluctuation. Figure 22 shows the time series of velocity components u'_1/u_* and u'_2/u_* at the centreplane of

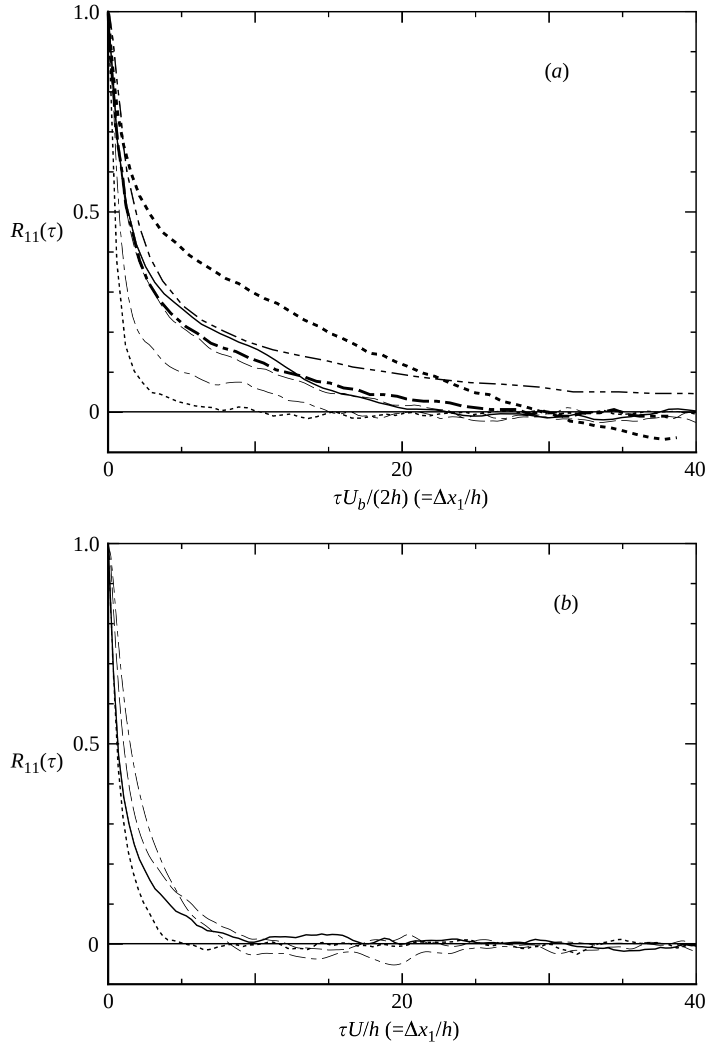

FIGURE 21. Auto-correlation coefficient of $u'_1(t)$. (*a*) At channel centre. (*b*) At $x_2{}^+ = 15$. Couette flow: ——, $Re_* = 192$; – – – –, $Re_* = 100$; —-—, $Re_* = 52$ by Komminaho *et al.*; ----, $Re = 3360$ and ——-—— , $Re = 1240$ by Tillmark & Alfredsson. Poiseuille flow: ----, $Re_* = 191$; —-—, $Re_* = 97$.

C-flow against $t_* = tu_*^2/\nu$. The streamwise component u'_1/u_* shows slow fluctuation with a large amplitude, indicated by a chain dot line, in addition to the conventional turbulent motion. In the figure, a size of $T^+ = 600$ is given as a reference time scale for this fluctuation. Such slow and large fluctuations appear only on u'_1 for C-flow, but not on the other components, or of course, on those of P-flow. The pre-multiplied power spectrum $\omega^+ E_{11}^+(\omega^+)$ of this u'_1 at the centre is shown in figure 23. Next to the lower end of the (-1) power range (constant-$\omega^+ E_{11}^+(\omega^+)$ range), a broadband peak at $\omega_p^+ \sim 0.01$ appears that corresponds to the time scale of $T^+ = 600$ shown in figure 22. The peak frequency ω_p can be scaled better by outer scales than inner scales as $\omega_p \risingdotseq (0.05 \sim 0.07) U_b/h$.

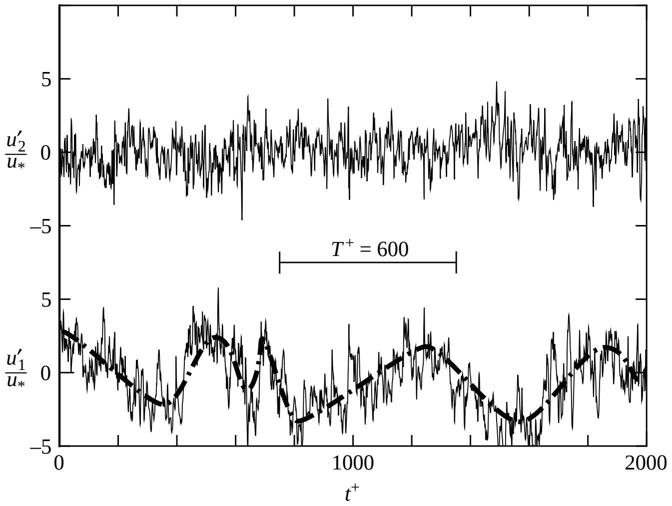

FIGURE 22. Time series of u'_1 and u'_2 signals of Couette flow ($Re_* = 192$) at $x_2 = h$ in $x_1/(2h) = 157$ section.

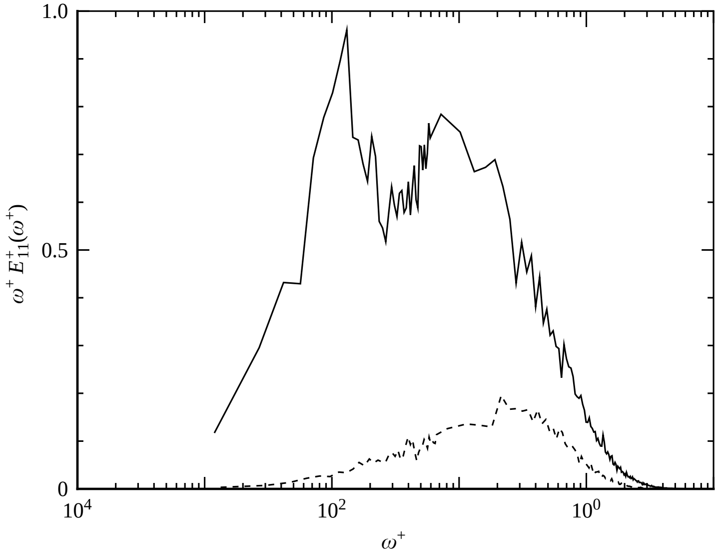

FIGURE 23. Pre-multiplied power spectrum $\omega^+ E_{11}{}^+(\omega^+)$ of u'_1 at channel centre. ——, Couette flow ($Re_* = 192$); - - - -, Poiseuille flow ($Re_* = 191$).

As described above, the wavy pattern of $\tilde{u}_1$ is sensitive to the inlet condition and it is not easy to control every detail to obtain reproducible data. To tackle this problem we introduced an artificial disturbance using a small thin plate placed at $x_3/(2h) = -3$ parallel to the flow at the inlet section. This plate introduces a wake component to C-flow as seen in the spanwise variation of U_c at $x_1/(2h) = 5.6$ shown in figure 24, which develops into a wavy pattern of U_c at the downstream section. This shows that large-scale vortices are developing in C-flow. In this case, the wavy variation of U_c in the spanwise direction is about $\pm 5\,\%$ at $x_2/(2h) = 157$, which is five times as large as the case without disturbance, figure 3. It is conjectured that the fluctuation of the

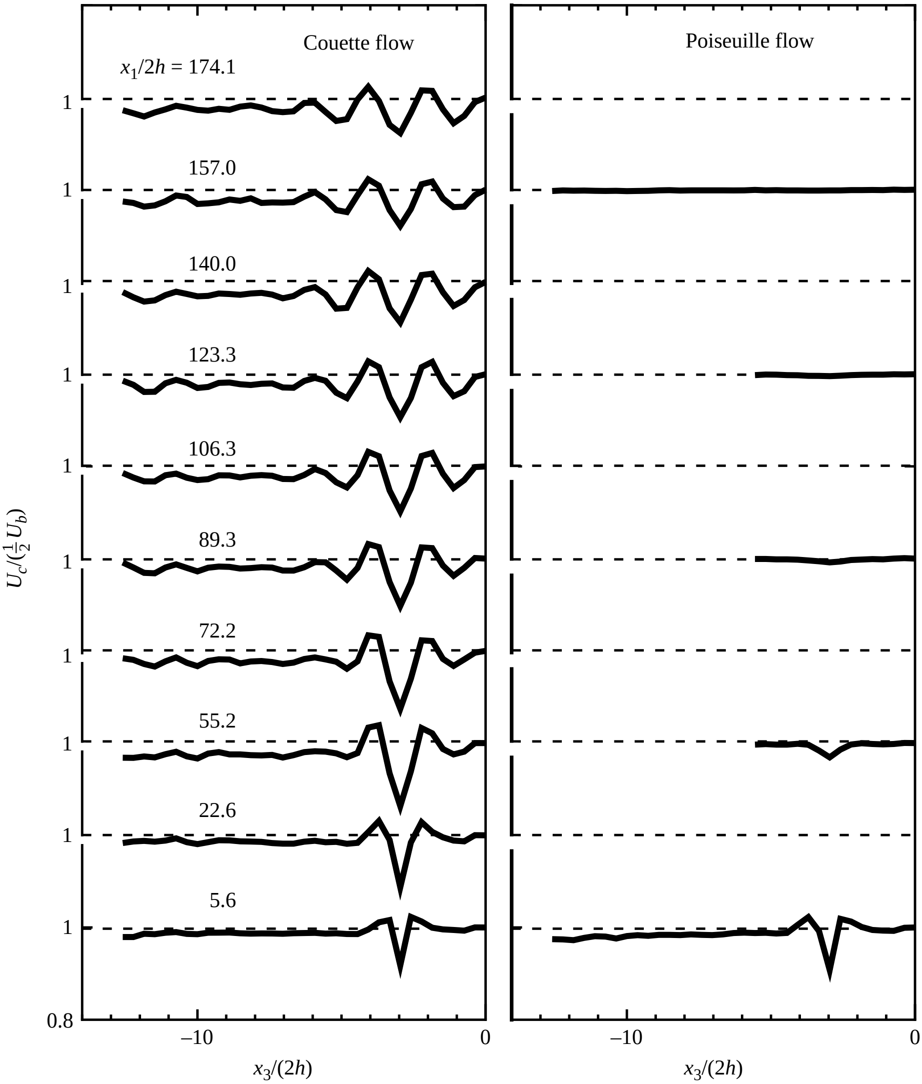

FIGURE 24. Development of wavy variation of U_c in downstream section at $Re = 3750$. Left-hand side is for Couette flow and right-hand side is for Poiseuille flow.

large longitudinal vortices is reduced by the introduction of the inlet disturbance. These rather quiet vortices make it easier to study the vortex characteristics and its effect on the flow field. In P-flow, however, the same wake at the inlet section soon decays, and two-dimensional Poiseuille flow is recovered in the downstream section. Figure 25 shows the velocity vector $\tilde{u}_2\boldsymbol{j} + \tilde{u}_3\boldsymbol{k}$ at $x_1/(2h) = 157$, where $\boldsymbol{j}$ and $\boldsymbol{k}$ are unit vectors in the x_2- and x_3-directions, respectively. A pair of counter-rotating vortices extending the entire channel width can be seen. The vortex components $\tilde{u}_2$ and $\tilde{u}_3$ are not large, only a few percent of U_b (given by the reference arrow in the figure). This is consistent with the results of Komminaho *et al.* (1996). The development of streamwise vorticity of the vortex pair at its core, $\tilde{\zeta}_1 = (\partial\tilde{u}_2/\partial x_3 - \partial\tilde{u}_3/\partial x_2)$, along the streamwise direction is shown in figure 26. Because of the limited number of measurements of $\tilde{u}_2$ and $\tilde{u}_3$ in the spanwise direction, the estimated value of $\tilde{\zeta}_1$ in the

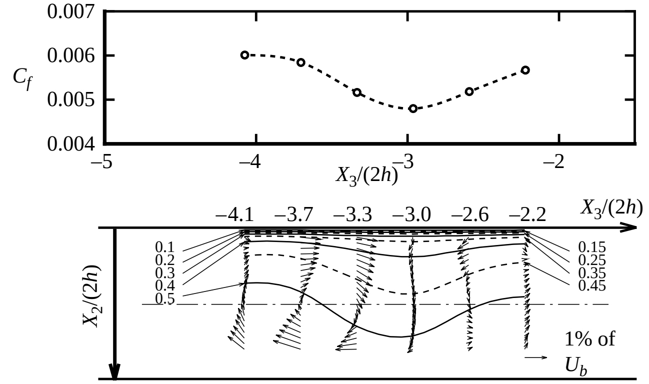

FIGURE 25. Velocity vectors at $x_1/(2h) = 157$ together with variation of wall friction coefficient in spanwise direction for $Re_* = 192$. Lines are equi-velocity contour of U_1/U_b.

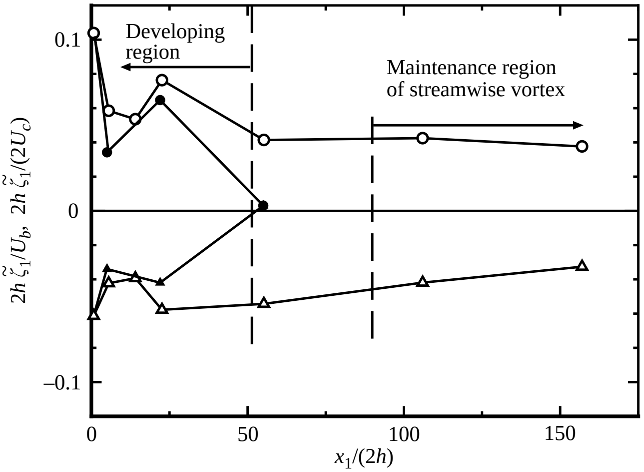

FIGURE 26. Development of streamwise vorticity at the vortex core in the downstream direction. Open symbols are for Couette flow and solid symbols are for Poiseuille flow. Circles and triangles are for positive and negative vortexes, respectively.

figure should be viewed with some reservation. We can obtain the qualitative change of $\tilde{\zeta}_1$ along $x_1/(2h)$. Up to $x_1/(2h) = 52$, $\tilde{\zeta}_1$ changes in a complex manner for both C- and P-flows. For P-flow, $\tilde{\zeta}_1$ decays almost completely at $x_1/(2h) = 52$. For C-flow, however, $\tilde{\zeta}_1$ becomes nearly constant in the farther downstream section. Considering that a developed C-flow is obtained at $x_1/(2h) = 90$, we believe that the region in which the streamwise vortex in C-flow is maintained is $x_1/(2h) \geqslant 90$. The following discusses the results in the maintenance region.

The large longitudinal streamwise vortices induce three-dimensionality in the C-flow. Convection of high (near the moving wall) or low (near the stationary wall) streamwise component of velocity by the vortex motion makes the equi-velocity contour wavy in the spanwise direction, as shown in figure 25. Even though the velocity of the vortex motion itself is low, the convection effect on the velocity U_1 is large. The skin friction coefficient $C_f = 2\tau_w/(\rho U_c^2)$ changes about 20 % sinuously in the spanwise direction due to velocity variation. Also the turbulence intensity u_1 varies sinuously

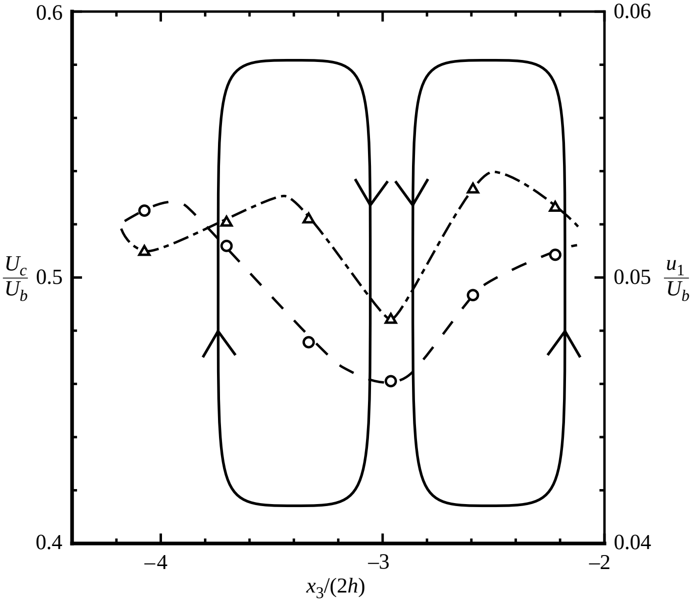

FIGURE 27. Spanwise variation of U_c/U_b and u_1/U_b at $x_2=h$ in relation to vortex motion. The vortex pattern illustrated is not the actual pattern, it is shown to indicate the spatial position and direction of the motion. ○, U_c/U_b; △, u_1/U_b.

along the x_3-direction, i.e. it is larger in the core than in other areas. Figure 27 summarizes the spanwise variation of U_c and u_1 with respect to the vortex motion. Turbulence intensity has its maximum at the positions of the largest mean velocity gradient $(\partial U_c/\partial x_3)_{\mathrm{Max}}$ and its minimum at $\partial U_c/\partial x_3=0$. The vortex pattern schematically shown is time averaged for the fluctuating vortex. The probable explanation of the u_1 and U_c distributions is given as follows, using a simple kinematic model of the vortex motion. As the vortex fluctuates in the spanwise direction around its mean position, it is accompanied by the velocity field around it. Provided that the vortex fluctuation is a simple harmonic with angular frequency ω, and the amplitude A_3 is not large compared with $2h$, the velocity fluctuation u_1'' due to this fluctuation can be expressed as

$$u_1'' = A_3\frac{\mathrm{d}U_c}{\mathrm{d}x_3}\sin\omega t. \tag{20}$$

Together with the ordinary turbulent motion u_1', the intensity of the fluctuating velocity leads to

$$\left\{\overline{(u_1'+u_1'')^2}\right\}^{1/2} = \left\{\overline{u_1'^2} + 0.5\left(A_3\frac{\mathrm{d}U_c}{\mathrm{d}x_3}\right)^2\right\}^{1/2}. \tag{21}$$

Here, the correlation between the turbulent motion and the harmonic oscillation is assumed to be zero. Using the data for $\mathrm{d}U_c/\mathrm{d}x_3$ and u_1/U_b at the peak and lowest positions of the turbulence intensity shown in figure 27, the amplitude can be estimated as $A_3/(2h)=0.28$. Although this is a rough estimation, it suggests that the intensity of the fluctuating velocity changes with $\mathrm{d}U_c/\mathrm{d}x_3$, as shown in figure 27.

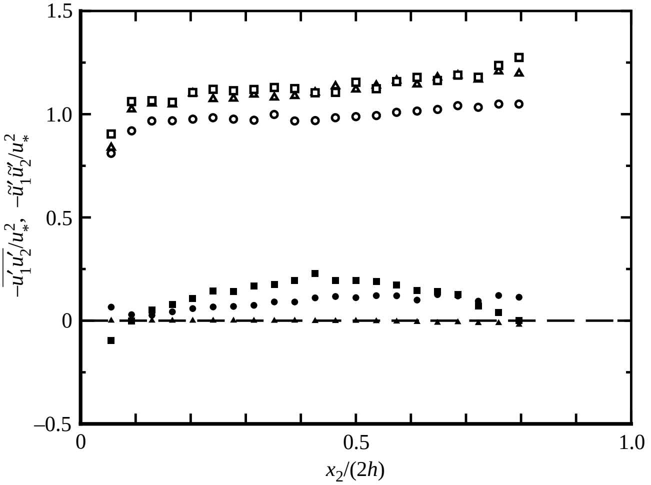

FIGURE 28. Distribution of shear stress due to turbulent motion and the wavy velocity component. Open symbols are for Reynolds shear stress and solid symbols are for wavy component. Spanwise position $x_3/(2h)$: circle, −2.2; triangle, −2.6; square, −3.0. ($Re_* = 192$, $x_1/(2h) = 157$).

Provided that the velocity is decomposed as in equation (19), the shear stress τ can be given as

$$\tau = \rho\nu\frac{\mathrm{d}U_1}{\mathrm{d}x_2} - \rho\overline{u_1'u_2'} - \rho\tilde{u}_1\tilde{u}_2. \tag{22}$$

The third term indicates the momentum transport by the fluctuating component. Figure 28 shows the distributions of the Reynolds shear stress and $-\rho\tilde{u}_1\tilde{u}_2$ at various spanwise positions. Because of the three-dimensional flow configuration induced by the vortex motion, the sum of the last two terms $(-\rho\overline{u_1'u_2'} - \rho\tilde{u}_1\tilde{u}_2)$ is not necessarily constant in the x_2-direction, as is shown in the figure. The wavy component $-\rho\tilde{u}_1\tilde{u}_2$ is basically positive and its profile differs significantly in the spanwise position, i.e. the relative position with respect to the vortex core. Along a line normal to the wall through the vortex core, it takes a minimum value of zero because $\tilde{u}_2 = 0$ in this region. The maximum value of $-\rho\tilde{u}_1\tilde{u}_2$ is about one quarter of the Reynolds shear stress.

The transport equation of the kinetic energy of the wavy component averaged in the spanwise direction $\langle\tilde{q}^2/2\rangle = \langle\tilde{u}_i\tilde{u}_i/2\rangle$ can be derived as follows, by assuming that $\tilde{u}_i$ is periodic in the spanwise direction and that the flow is fully developed (all variables are normalized by U_b and $2h$):

$$\begin{aligned}
0 = \quad & \underbrace{-\frac{\partial\langle\tilde{u}_2(\tilde{p}+\tilde{q}^2/2)\rangle}{\partial x_2}}_{\mathrm{II}} \quad \underbrace{-\langle\tilde{u}_i\tilde{u}_2\rangle\frac{\partial\langle U_1\rangle}{\partial x_2}}_{\mathrm{III}} \\
& \underbrace{-\frac{\partial\langle\tilde{u}_i\overline{u_i'u_2'}\rangle}{\partial x_2}}_{\mathrm{IV}} \quad \underbrace{+\left\langle\overline{u_i'u_2'}\frac{\partial\tilde{u}_i}{\partial x_2}\right\rangle + \left\langle\overline{u_i'u_3'}\frac{\partial\tilde{u}_i}{\partial x_3}\right\rangle}_{\mathrm{V}} \\
& \underbrace{+\frac{1}{4Re}\frac{\partial}{\partial x_2}\left\langle\tilde{u}_i\frac{\partial\tilde{u}_i}{\partial x_2}\right\rangle}_{\mathrm{VI}} \quad \underbrace{-\frac{1}{4Re}\left\langle\frac{\partial\tilde{u}_i}{\partial x_j}\frac{\partial\tilde{u}_i}{\partial x_j}\right\rangle}_{\mathrm{VII}}
\end{aligned} \tag{23}$$

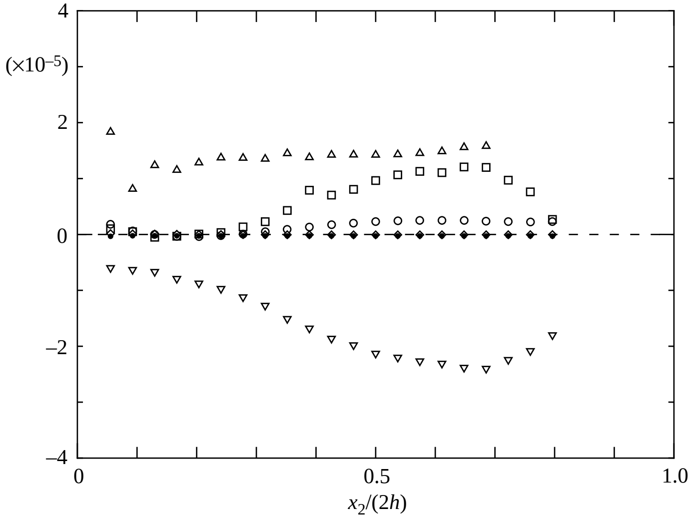

FIGURE 29. Kinetic energy budget of wavy velocity component. $Re_* = 192$, $x_1/(2h) = 157$. Term in equation (23): ○, II; △, III; □, IV; ▽, V; ◇, VI; ●, VII.

Term III is the production term of $\langle \tilde{q}^2/2 \rangle$ by the shear stress $-\rho \tilde{u}_1 \tilde{u}_2$ from mean flow, while terms V are the transfer of kinetic energy from the wavy to the turbulent component by Reynolds shear stress. The energy budget of the above equation is given in figure 29. Terms including $\tilde{p}$ or $\overline{u_2' u_3'}$ cannot be measured and are not contained in the figure. Viscosity related terms, VI and VII, are small enough to be neglected. The production term III has a positive value, obtaining wavy component energy from the mean flow, and term V has a negative value of the same size, releasing its energy to the turbulent motion.

5. Concluding remarks

The mean velocity profile and turbulence characteristics of plane turbulent Couette flow from low to high Reynolds number as well as the large streamwise vortex structures are experimentally studied. The important differences of Couette flow from conventional wall turbulent flow, such as Poiseuille flow, are (i) no shear stress gradient prevailing in the entire channel, and (ii) the existence of large longitudinal vortices in the central part of the channel. These two differences are closely related to the specific features of the Couette flow studied here.

Since the Couette flow is free from the shear stress gradient, the Reynolds number is a unique parameter of the flow, unlike in Poiseuille flow where the μ-parameter effect appears implicitly. Because the Couette flow is realized at $|\mu| \rightarrow \infty$ and the relation $\mu = -Re_*$ holds for Poiseuille flow, both Couette flow and high-Reynolds-number Poiseuille flow are similar, even though the Reynolds number of the Couette flow is not high, as far as the wall region is concerned. For Couette flow, the Reynolds number effect on mean velocity and turbulent intensity profiles is quite small in the wall region. The low-Reynolds-number effect on the profiles is noticeable only when Re_* is less than 150. The effect appears as the relative size of the viscous length scale with respect to h increases, and the h-effect appears in the buffer region. The additive constant B of the log law decreases somewhat and the peak value of turbulence intensity u_{1p}^+ drops sharply as Re_* decreases. These low-Reynolds-number effects are significantly different from Poiseuille or turbulent boundary layer flows. The outer boundary of the log-law area is $x_{2u}^{+} = (0.6 - 0.8)Re_*$, which is two or three times as large as that for Poiseuille flow. The sweep contribution to the Reynolds shear stress in Couette flow is stronger than in Poiseuille flow because of higher turbulence activity in the central area of the Couette flow.

Because of the non-zero mean shear in the turbulent core region, the defect law is no longer Re_*-independent, but its velocity slope Rs increases with Re_* and seems to asymptotically approach a constant value of 5 when $Re* > 500$.

There is some mechanism, not clarified yet, in Couette flow that can sustain large-scale streamwise vortex structures. Because of these vortex structures, there is a long surviving correlation $R_{11}(\tau \text{ or } \Delta x_1)$ in Couette flow, and the streamwise distance of zero correlation is 3 times as long as that of Poiseuille flow at the channel centre. Because the large-scale vortices are not stationary but fluctuating around an average position, a slow fluctuation with large amplitude appears in the streamwise velocity component at a fixed point, and the power spectrum has a peak at the lower end (−1) of the power area, $\omega_p \risingdotseq (0.05 \sim 0.07)U_b/h$. The disturbance at the inlet section makes the large longitudinal vortices rather stationary and the vortex effects on the flow are pronounced. The large-scale streamwise vortices introduce a three-dimensional configuration into Couette flow. The skin friction coefficient varies 20 % in the spanwise direction, and the shear stress is no longer necessarily constant.

REFERENCES

Andersson, H. I., Bech, K. H. & Kristoffersen R. 1992 On diffusion of turbulent energy in plane Couette flow. *Proc. R. Soc. Lond.* A **438**, 477–484.

Antonia, R. A., Teitel, M., Kim, J. & Brown, L. W. B. 1992 Low-Reynolds-number effects in a fully developed turbulent channel flow. *J. Fluid Mech.* **236**, 579–605.

Bech, K., Tillmark, N., Alfredsson, P. H. & Andersson, H. I. 1995 An investigation of turbulent plane Couette flow at low Reynolds numbers. *J. Fluid Mech.* **286**, 291–325.

Bhatia, J. C., Durst, F. & Jovanovic, J. 1982 Correction of hot-wire anemometer measurements near walls. *J. Fluid Mech.* **122**, 411–431.

Carruthers, D. J., Fung, J. C. H., Hunt, J. C. R. & Perkins, R. J. 1991 The emergence of characteristic (coherent?) motion in homogeneous turbulent shear flow. *Turbulence and Coherent Structures* (ed. O. Metais & M. Lesieur), pp. 29–44. Kluwer.

El Telbany, M. M. M. & Reynolds, A. J. 1980 Velocity distribution in plane turbulent channel flows. *J. Fluid Mech.* **100**, 1–29.

El Telbany, M. M. M. & Reynolds, A. J. 1982 The Structure of Turbulent Plane Couette Flow. *Trans. ASME: J. Fluids Engng* **104**, 367–372.

Gad-el-Hak, M. & Bandyopadhyay, P. R. 1994 Reynolds number effects in wall-bounded turbulent flows. *Appl. Mech. Rev.* **47**, 307–365.

Hamilton, J., Kim, J. & Waleffe, F., 1995 Regeneration mechanism of near-wall turbulence structures. *J. Fluid Mech.* **287**, 317–348.

Hussain, A. K. M. F. & Reynolds, W. C. 1975 Measurements in fully developed turbulent channel flow. *Trans. ASME: J. Fluids Engng* **97**, 568–580.

Kim, J., Moin, P. & Moser, R. 1987 Turbulence statistics in fully developed channel flow at low Reynolds number. *J. Fluid Mech.* **177**, 133–166.

Kitoh, O., Nakabayashi, K. & Katoh, Y. 1995 Law of the wall under effect of shear stress gradient. *Proc. 6th Asian Congress of Fluid Mech. Singapore*, pp. 1412–1415.

Komminaho, J., Lundbladh, A. & Johansson, A. V. 1996 Very large structure in plane turbulent Couette flow. *J. Fluid Mech.* **320**, 259–285.

Kuroda, A. 1990 Direct numerical simulation of Couette-Poseuille turbulent flow. Dissertation, Tokyo University.

LEE, M. J. & KIM, J. 1991 The structure of turbulence in a simulated plane Couette flow. *Proc. 8th Symposium on Turbulent Shear Flows, Munich*, paper 5-3.

LEE, M. J., KIM, J. & MOIN, P. 1990 Structure of turbulence at high shear rate. *J. Fluid Mech.* **216**, 561–583.

MACCARTHY, J. H. 1964 Steady flow past non-uniform wire grids. *J. Fluid Mech.* **19**, 491–512.

NAKABAYASHI, K., KITOH, O., ADACHI, M. & IKEYA, T. 1994 Turbulence structure in plane turbulent couette flow. *Trans. JSME* **60**, 578, 3249–3255.

NAKABAYASHI, K., KITOH, O., IWATA, H., KATO, E. & UEHARA, T. 1988 Basic study on turbulent lubrication (1st report, Turbulent plane Couette flow). *Trans. JSME* **54**, 499, 547–552.

NAKABAYASHI, K., KITOH, O. & KATOH, Y. 1995 Mean velocity profiles of Couette·poiseuille-type turbulent flow. *Trans. JSME* **61**, 589, 3122–3129.

NAKABAYASHI, K., KITOH, O. & KATOH, Y. 2004 Law of velocity distribution and turbulence characteristics of Couette-Poiseuille turbulent flows. *J. Fluid Mech.* **507**, 43–69.

NAGANO, Y., TAGAWA, M. & TSUJI, T. 1991 Effects of adverse pressure gradients on mean flows and turbulence statistics. In *Proc. 8th Symp. Turbulent Shear Flows, Munich*, 2-3, pp. 1–6.

PATEL, V. C. & HEAD, M. R. 1969 Some observations on skin friction and velocity profiles in fully developed pipe and channel flows. *J. Fluid Mech.* **38**, 181–201.

PERRY, A. E. & ABELL, C. J. 1975 Scaling laws for pipe-flow turbulence. *J. Fluid Mech.* **67**, 257–271.

REICHARDT, T. 1959 Gesetzmässigkeiten der geradlinigen turbulenten Couetteströmung. *Mitt. Maxplanck-Institut für Strömungsforschung*, no. 22, Göttingen.

ROBERTSON, J. M. & JOHNSON, H. F. 1970 Turbulence structure in plane Couette flow. *J. Engng Mech. Div. ASCE* **96**, 1171–1182.

TAVOULARIS, S. & KARNIK, U. 1989 Further experiments on the evolution of turbulent stresses and scales in uniformly sheared turbulence. *J. Fluid Mech.* **204**, 457–478.

TILLMARK, N. & ALFREDSSON, P. H. 1992 Experiments on transition in plane Couette flow. *J. Fluid Mech.* **235**, 89–102.

TILLMARK, N. & ALFREDSSON, P. H. 1994 Structure in turbulent plane Couette flow obtained from correlation measurements. *Advances in Turbulence V* (ed. Benzi), pp. 502–507. Kluwer.

WEI, T. & WILLMARTH, W. W. 1989 Reynolds-number effects on the structure of a turbulent channel flow *J. Fluid Mech.* **204**, 57–95.